Chapter 2

The Ring Imaging Cherenkov detector for CLAS12

To perform QCD measurement with flavor sensitivity, an efficient system to identify the hadrons in the final state is fundamental. This Chapter introduces the CLAS12 spectrometer focusing on the PID system and describes the Ring Imaging Cherenkov (RICH) detector. Particularly, the author was involved in the assembly and commissioning of the second module, in the efficiency study of the first module, and in the first physics analysis carried out using the RICH data. The first two of these activities are described in this Chapter.

2.1 The CLAS12 spectrometer at Jefferson Lab

The Thomas Jefferson National Accelerator Facility (JLab) is one of the most important laboratories dedicated to nuclear physics research that is carried out using the electron beam provided by the Continuous Electron Beams Accelerator Facility (CEBAF) and different apparatuses realized in four experimental halls. The JLab site is shown in Figure 2.1. The high intensity, highly polarized, 12 GeV electron beam permits to perform sophisticated measurements aiming to probe and possibly extend the Standard Model of particle physics via precise parity violation measurement, light dark matter searches, and exotic particle discovery, exploiting the peculiarities of the four halls. A scheme of CEBAF is represented in Figure 2.2.

The experimental Hall B hosts the CEBAF Large Acceptance Spectrometer for operation at 12 GeV (CLAS12)[31], a spectrometer developed by an international collaboration of 48 institutions. CLAS12 is based on a dual-magnet system, constituted by a torus magnet and a solenoid magnet, and it is designed to provide efficient detection of charged and neutral particles over a large fraction of the solid angle. The main tasks of the CLAS12 physics program are:

- Nucleon structure studies using exclusive and semi-inclusive deep in-

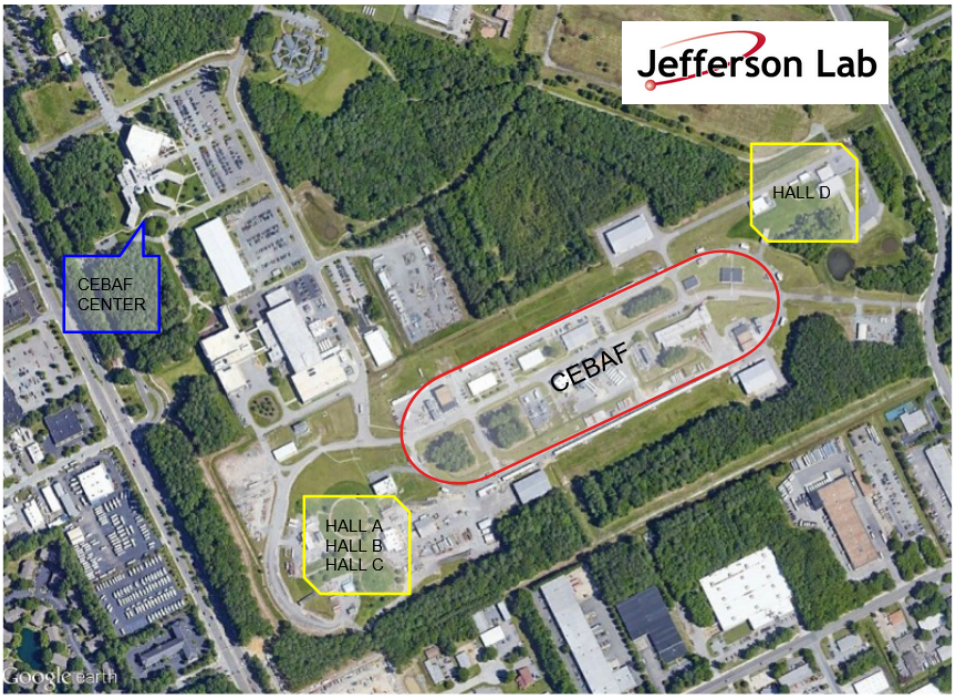

Figure 2.1: The JLab site

Figure 2.2: The CEBAF and experimental halls scheme

elastic scattering processes by mapping the Generalized Parton Distributions (GPDs)[1] and Transverse-Momentum-Dependent distributions (TMDs);

- Precision measurement of structure functions and forward parton distribution at high x_B;
- Elastic and transition form factors at high momentum;
- Hadronization and color transparency;
- Hadron spectroscopy, studying heavy baryons and mesons with ordinary and exotic quantum numbers.

The magnets

The solenoid (Figure 2.3a) is made by self-shielded superconducting coils surrounding the beamline and used to generate a magnetic field primary in the beam direction. This design allows us to achieve the physics requirements of shielding the Moeller electron background, tracking particles with large angles, and providing a uniform field in the center to operate dynamically polarized proton and deuteron targets. The solenoid generates a 5 T field at its center at the maximum current.

The torus (Figure 2.3b) magnet comprises six identical superconducting coils, symmetrically arranged to obtain a toroidal field around the beamline. The geometrical coverage seen from the target is between 5° and 40°. The peak field is 3.58 T, while the field is zero at the center for reasons of symmetry.

2.1.1 The detector

CLAS12 can be divided into the Central Detector (CD) and the Forward Detector (FD).

The Central Detector

The CD is designed to detect particles covering the polar angle between 35° and 125° and almost the whole azimuthal angle. The CD is placed inside the solenoid magnet. The tracking and the measure of the momentum are provided by the Central Vertex Tracker (CVT), while the charged particle identification is entrusted to the Central Time-Of-Flight (CTOF). Moreover, the CD includes two neutron detectors, the Central Neutron Detector (CND) and the Back Angle Neutron Detector (BAND). These detect neutrons with momentum up to 1.25 GeV and polar angle up to 175°.

[1] GPDs are a different way of accessing the nucleon structure. They are like tomographic slices of the form factors at a fixed value of the momentum fraction x_B

(a) CLAS12 solenoid **(b)** CLAS12 torus

Figure 2.3: The CLAS12 superconducting magnets.

The Forward Detector

The Forward Detector (FD) covers polar angles between 5° and 35°, with tracking, particle identification, and momentum measurement provided by different detectors. The FD structure is based on the torus magnet, so it is divided into six sectors that are identical in dimensions and almost identical in composition. All the sectors include three regions of Drift Chamber (DC) for tracking and two calorimeters, the Electromagnetic Calorimeter (EC) and Pre-shower Calorimeter (PCAL) for identification and kinematical reconstruction of electrons, photons, and neutrons. The only differences between sectors regard the Particle Identification (PID) components. Indeed, all six are equipped with a High Threshold Cherenkov Counter (HTCC) and a Forward Time-Of-Flight (FTOF), four sectors host a Low Threshold Cherenkov Counter (LTCC), and the other two a Ring Imaging Cherenkov (RICH) detector; more details about the PID are discussed in the following. Moreover, the FD includes the Forward Tagger (FT) to extend the capability of detecting electrons and photons at very forward polar angles between 2.5° and 4.5°, consisting of a calorimeter, a hodoscope, and a micro-strip gas tracker.

The FD Particle Identification

The PID plays a crucial role in QCD studies with flavor sensitivity, particularly the capability to distinguish charged hadrons and leptons. Indeed,

aiming to perform SIDIS measurements, the precise identification of the final ~~states~~ acquires great importance. The following detectors concur in the PID:

- The Forward Time-Of-Flight (FTOF) measures the time-of-flight of charged particles from the production target. The system is designed to reach an average time resolution of 80 ps to distinguish pions and kaons up to 3 GeV.
- The Low Threshold Cherenkov Counter (LTCC) is a Cherenkov counter that uses C_4F_{10} as a radiator; it allows the tag of the charged pions up to 3.5 GeV.
- The High Threshold Cherenkov Counter (HTCC) separates the electrons and positrons with momenta below 4.9 GeV from charged hadrons. It operates in dry CO_2 gas at 1 atm pressure.
- Two Ring Imaging Cherenkov (RICH) detectors were added (the first in 2018 and the second in 2022) in two opposite sectors to improve the identification of charged kaons in higher momentum range inaccessible with the FTOF and LTCC. They are based on the measurement of the Cherenkov angle of the photons emitted by the charged particle passing through an aerogel radiator, which, combined with the kinematic information, allows the separation of the hadron species.

A scheme of the RICH and LTCC positions is shown in Figure 2.4. The author was directly involved in the assembly of the second module of the RICH, in the efficiency studies of the first module, and in the first analysis of SIDIS based on the RICH ~~to identify the kaons~~.

2.2 The CLAS12 Ring Imaging Cherenkov

In 2018, a first Ring Imaging Cherenkov (RICH) detector [32] was incorporated into the CLAS12 spectrometer at JLab. A RICH ~~exploits~~ the Cherenkov photons produced by a charged particle crossing a radiator with a speed greater than the speed of light in that medium to identify the velocity of the particle. This information, combined with the momentum measured by other detectors, allows to identify the mass of the particle. The Cherenkov effect is described by

$$\cos\theta_{Ch} = \frac{1}{\beta n(\lambda)} \tag{2.1}$$

where θ_{Ch} is the opening angle of the photon from the particle trajectory, β is the particle's speed, and $n(\lambda)$ is the refractive index of the medium depending on the wavelength. After a gap region, the projection of the Cherenkov ~~cone~~ is the so-called "ring", which has to be detected by light detectors operating in single-photon mode. A generic RICH functioning scheme is shown in

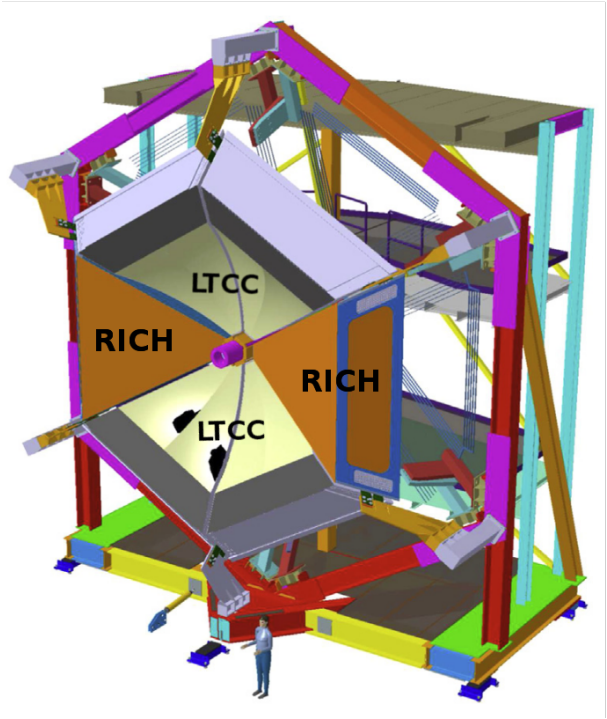

Figure 2.4: Scheme of the RICH and LTCC detectors position in CLAS12.

Figure 2.5a. The CLAS12 RICH was explicitly designed to facilitate efficient kaon identification in the momentum range between 3 GeV/c and 8 GeV/c. Indeed, the original PID system based on FTOF, LTCC, and HTCC does not provide sufficient separation in this momentum range between kaons, pions, and protons for effective SIDIS studies on kaons. In 2022, a second module was installed, identical to the first. Figure 2.15b shows CLAS12 with the two RICH modules.

2.2.1 RICH design

According to the CLAS12 Monte Carlo studies, the kaons identification needs to achieve a rejection factor for pions in the order of $1:500$, corresponding to a separation of 4σ between pions and kaons. As shown in Figure 2.6, the only possible radiator is the silica aerogel, which has a very low macroscopic density and a refractive index between the gas and the liquids. The RICH has to ~~match~~ inside the Forward Carriage of CLAS12, which imposes several constraints: a projective geometry, a limited depth of 1.2 m, and $\sim 4.5\,\mathrm{m}^2$ entrance window~~s~~. Based on the simulation, the RICH is designed to integrate the aerogel radiator~~s~~, visible light photon detectors, and a focusing mirror system in a compact hybrid-optics design. The mirrors allow the reduction of the photon detector area to $\sim 1\,\mathrm{m}^2$, minimizing the cost and the impact on the

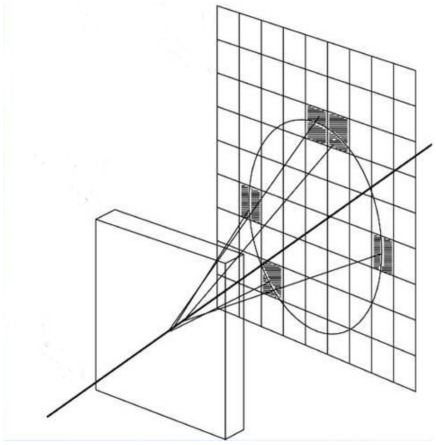

(a) Functioning scheme of a generic RICH detector

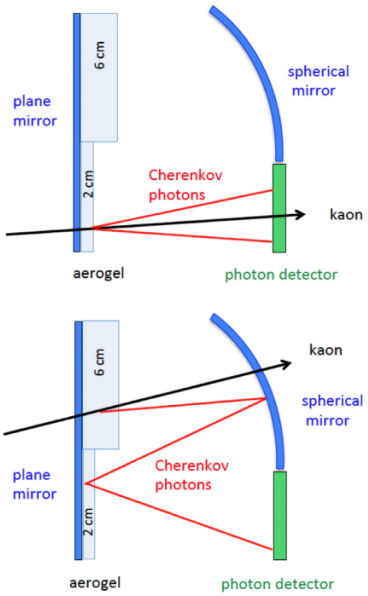

(b) On top direct imaging; on bottom imaging after one or more reflections on the mirrors.

Figure 2.5

downstream detectors. Depending on the polar angle of the incident particles, the photons can hit the photo-detection area directly, as shown in Figure 2.5b. To minimize the total material budget, the mechanical structure is made almost entirely of light materials, particularly carbon fiber. A complete detector scheme is shown in Figure 2.7.

2.2.2 The radiator

The radiator selected for the RICH was the silica aerogel, the only possible choice, as shown from the plot in Figure 2.6, where the expected Cherenkov angle for different hadrons is plotted as a function of the particle momentum. The aerogel is an amorphous solid network of SiO_2 nanosphere, and it has a very low macroscopic density and a refractive index intermediate between gas and liquid radiators. The aerogel was produced by Budker and the Boreskov Institute of Nuclear Physics (Russia), which made all the 102 tiles of different shapes and thicknesses needed for each detector module. The tiles were assembled into two sections. The first, made of one layer of 2-cm-thick tiles, covers the region between the beam pipe up to the polar angle of 17.5°. The second region covers the polar angle between 17.5° and 26° and is made of two layers of 3-cm-thick tiles. Most tiles are squared $20 \times 20\,\mathrm{cm}^2$ bricks, but triangular, trapezoidal, and pentagonal shapes became necessary on the edges

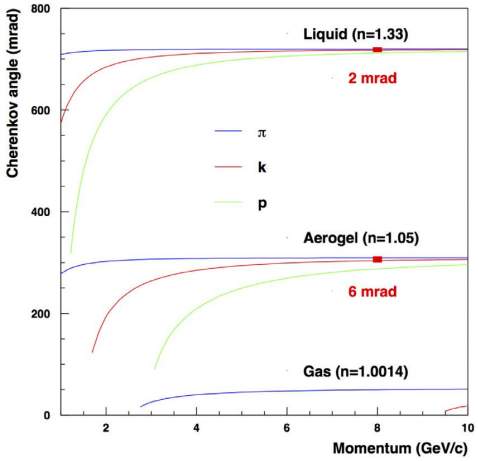

Figure 2.6: Expected Cherenkov angle for different hadron as a function of momentum for different radiators.

to cover the entire entrance window. Each tile was tested [25] to determine the side length, thickness, and surface planarity. Also, the optical parameters were measured, particularly the refractive index at the reference wavelength of 400 nm and the light transmission as a function of the wavelength. Using the Hunt parametrization [12], the parameters of transparency A_0, clarity C, and scattering length at 400 nm Λ_S were extracted. From these measurements, the expected mean photon yield is 19 photoelectrons (p.e.) for the 2-cm-thick layer and 25 p.e. for the 6-cm-thick layer.

2.2.3 The mirror system

According to the simulation, the mirror system was designed to minimize the loss of photons and direct most of them to the photon detector. A drawing of the entire mirror system is shown in Figure 2.8.

The spherical mirror

It comprises ten sub-mirrors produced by the *Composite Mirror Applications* company [50]. It covers a total surface of 3.6 m^2 and has a curvature radius of 2.7 m. This mirror is placed in front of the entrance window to collect the photons produced by particles entering with the larger polar angle. The accuracy of each sub-mirror spherical surface was quantified via the spot size measurement, illuminating the mirror with a point-like source and observing the size of the reflected spot with a CCD camera in its center. The size spot is quantified by D_0, the minimum diameter containing 90% of the reflected light, which is related to the angular resolution by

$$\sigma_\theta = \frac{D_0}{8R} \tag{2.2}$$

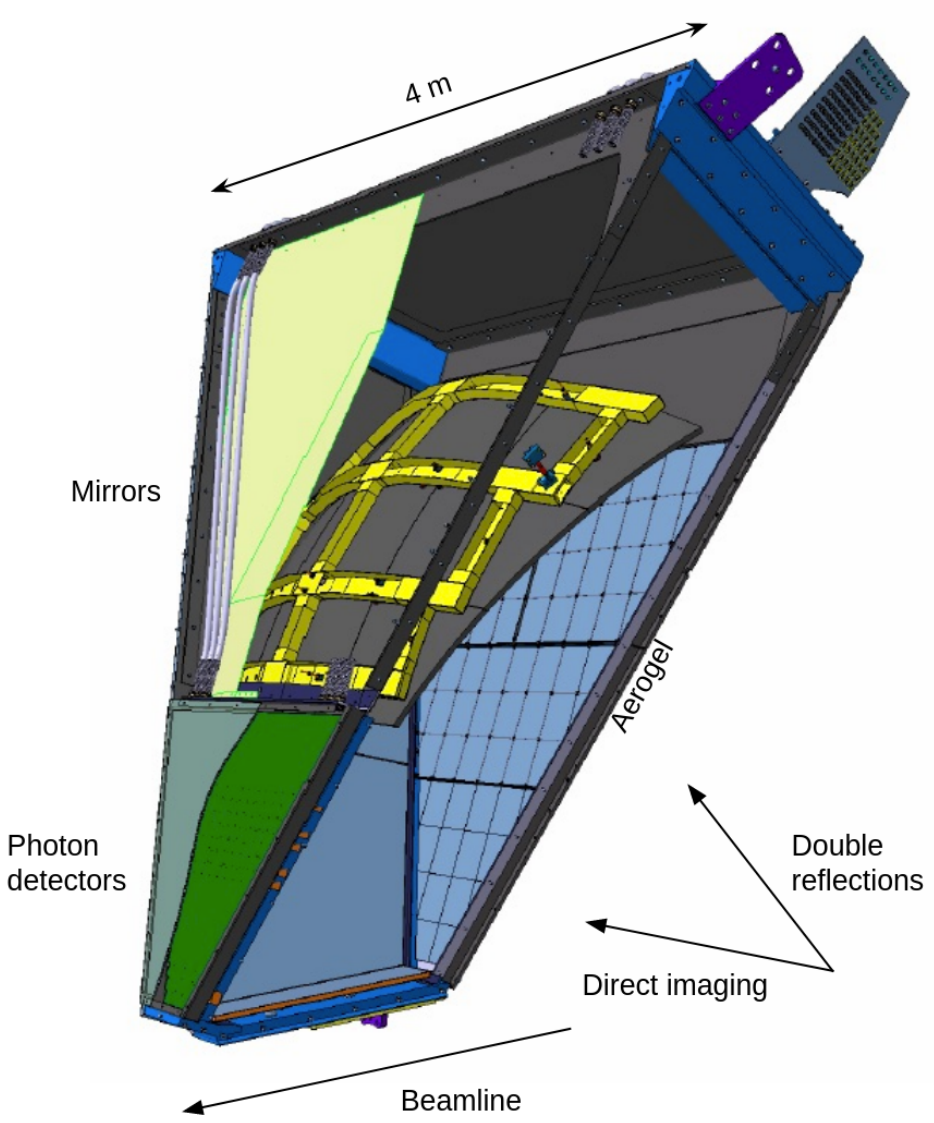

Figure 2.7: Sketch of the full RICH: the aerogel tiles, the structure supporting the spherical mirrors, and the photo-detection plane are indicated.

where R is the curvature radius. The mirror mechanical substrate is made by a sandwitch of two carbon fiber layers with a honeycomb core that achieves a high rigidity and a low material budget of $0.01X_0$. The mirrors were coated with a reflective SiO_2 layer by the *Evaporated Coating* company [51]. The reflectivity of the mirrors is measured to be between 88% and 90% in the $300 - 700\,\text{nm}$ wavelength range of interest.

The planar mirrors

There are seven planar mirrors, two placed on each side of the detector, one on the bottom, and two on the front panel supporting the aerogel, covering a total surface of $6.5\,\text{m}^2$. They were produced by the *Media Lario* company [52], which is used to work for terrestrial telescope applications. The mirrors are made of two skins of glass glued on an aluminum honeycomb core; the front mirror skins are 0.7 mm thick to reduce the mirror material budget to $\sim 0.01X_0$ in the detector acceptance, ~~and the other~~ mirror skins ~~are~~ 1.6 mm ~~thick~~. The reflectivity of the planar mirrors has been measured to be greater than 90% in the $300 - 700\,\text{nm}$ range of wavelength and shows a maximum of about 95% at 400 nm.

2.2.4 The photon detector

The mirrors ~~made it possible~~ to reduce the photo-detection area to $\sim 1\,\text{m}^2$, in the region close to the beamline where most of the particles are produced and ~~carrying~~ the most demanding high momenta.

The photo-sensor

To make imaging possible, the photo-sensor has to work efficiently in the Single PhotoElectron (SPE) regime and be sensitive to visible light (to match the aerogel emission spectrum). Moreover, it must have the spatial resolution required to achieve the designed angular resolution, provide an active area with minimal dead space, and be insensitive to the low torus fringe field where the RICH readout is located (estimated to be no more than 3.5 G). The Hamamatsu flat-panel Multi-Anode Photomultiplier Tube (MAPMT) H8500, an 8×8 array of $6 \times 6\,\text{mm}^2$ pixels covering a $5 \times 5\,\text{cm}^2$ area, was initially selected as photo-sensor. However, it was not ~~optimal~~ for the SPE regime. Just after the start of ~~the build of the first module of the RICH~~, Hamamatsu released the H12700 MAPMT, which has the same layout and an optimized dynode structure for ~~the~~ SPE. The first RICH combines 80 H8500 and 311 H12700 for 391 photo-sensors, while the second module is fully equipped with H12700. This configuration results in 25024 pixels covering the $\sim 1\,\text{m}^2$ trapezoidal active area of each RICH module. Figure 2.9a, shows a view of the MAPMTs side of the electronic panel.

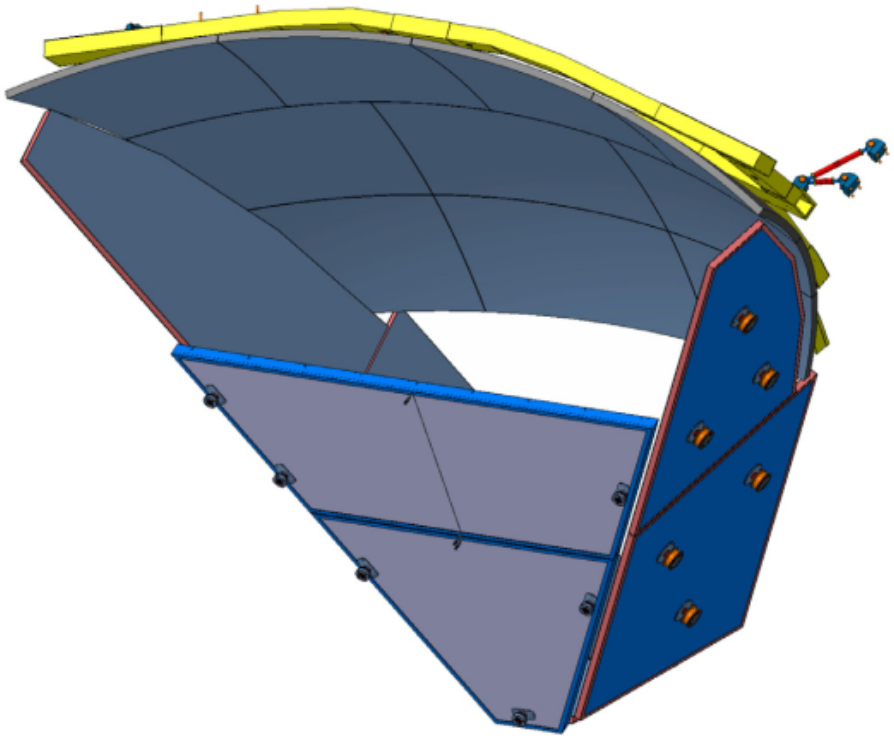

Figure 2.8: RICH mirror system draw. The spherical mirror has ten different spherical mirrors reflecting the light backward. Two mirrors upstream on the aerogel reflect the photons a second time in the direction of the MAPMTs, as shown in figure 2.5b. To minimize the photon loss, two planar mirrors on each side and one on the bottom surround the rest of the RICH module.

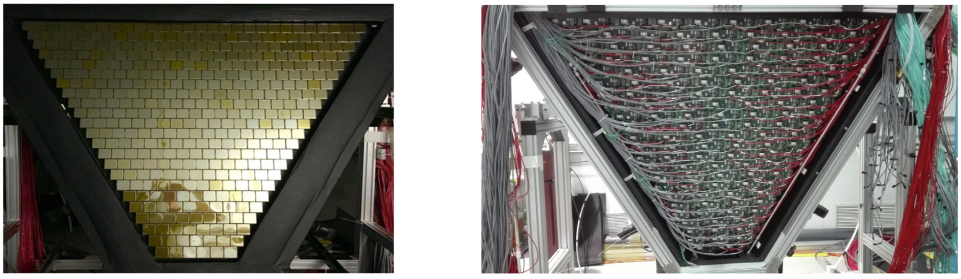

(a) MAPMTs side **(b)** Front-end electronic side

Figure 2.9: The RICH electronic panel.

The readout electronics

The front-end electronics is organized in compact modules called tiles serving two or three MAPMTs. The tile scheme is shown in Figure 2.10. The front-end electronics is intended to ensure a 100% efficiency at $\frac{1}{3}$ of the average photoelectron signal level, 1 to 4 gain spread compensation, and time resolution of the order of 1 ns to distinguish direct from reflected hits. Additionally, it has to sustain a 20 kHz trigger rate with 8 µs latency and negligible dead time. Three different boards make each readout unit:

- The adapter board provides the electrical connectivity of the sensors with the readout, preserving the light and gas tightness when the electronic panel is mounted in the detector. It also distributes the power to the MAPMTs, nominally −1000 V.

- The ASIC board mounts two or three Multi-Anode ReadOut Chip (MAROC) chips, a 64-channel microcircuit dedicated to processing MAPMTs signal.

- The FPGA board hosts a Xilinx7 FPGA chip responsible for configuring and reading the MAROC chips, distributing the trigger, and interfacing with the DAQ system.

To complete the readout system, three kinds of cable have been connected to each tile: the low-voltage cables to power the FPGA, the high-voltage cable to power the MAPMTs, and the optical fiber for the communication between the FPGA and the DAQ system. The last step to complete the electronic panel was to add a grounding grid, which attenuates the electronic noise, and the cooling system, based on a flow of compressed dry air that allows to maintain the temperature of the FPGA below the critical temperature of 75 °C. A picture of the full readout electronics of the RICH is reported in Figure 2.9b.

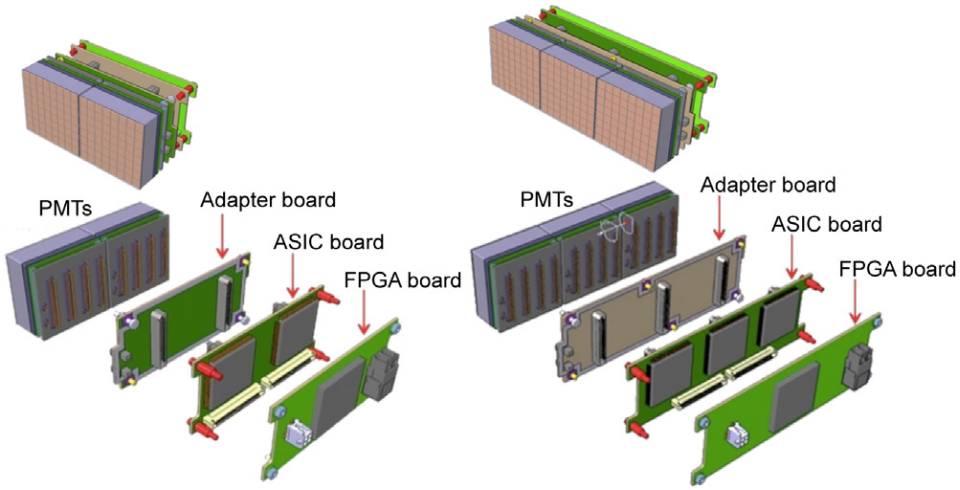

Figure 2.10: Scheme of the front-end electronic tiles serving two (left) or three (right) MAPMTs.

2.3 The assembly and commissioning of the second module of the RICH

In the spring of 2022, the author was directly involved in assembling the second module of the RICH, particularly concerning the electronic panel mounting and the installation of the detector inside the CLAS12 experiment. The assembling process before the installation was performed inside a clean room at JLab, and each subsystem was installed in the detector structure after the completion of the relative characterization tests. The expert of mechanics from INFN Frascati took care of the assembly of the RICH vessel (see Figure 2.12a), which has to sustain the entire detector structure. The spherical mirrors were characterized and then ~~placed~~ in their ~~sustain~~ structure inside the vessel, while the planar mirrors were directly p~~laced~~ on the vessel's walls (Figure 2.12d). The characterization includes measurements of the reflectivity in several points and of the ~~light~~ spot size. The spherical sub-mirrors were aligned using a point-like source and converging the reflected spot on the same point (Figure 2.12c). The hydrophobic aerogel was purged with a flux of nitrogen and mounted on the inner side of the frontal panel, in the section with (Figure 2.11a) and without (Figure 2.12b) mirrors. The INFN Ferrara team, including the author, worked mainly on the electronic panel, placing the adapter boards on the inner side and connecting them with the ASIC boards on the other side (Figure 2.12e). Then, they added the FPGA boards to the ASIC boards and cabled all the 138 tiles (Figure 2.12f). After completing this step, the 391 MAPMTs were put in place by members of the Ferrara team, JLab and Duquesne University. All the readout units were connected to the power and DAQ system and tested. Under the

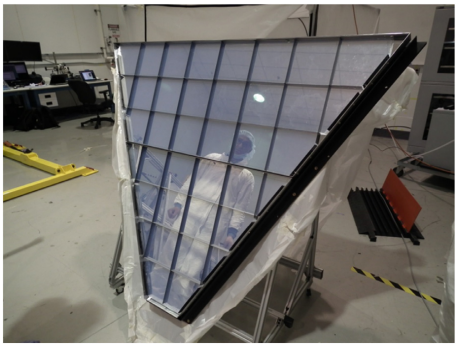

(a) The 2-cm-thick section of the aerogel mounted on the two frontal mirrors.

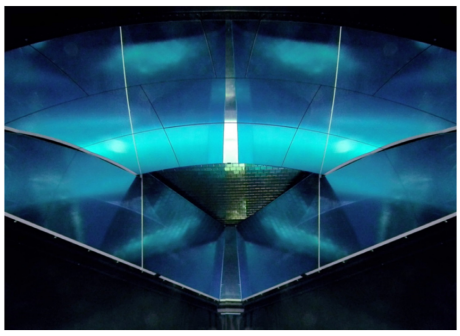

(b) Inside the RICH detector, the mirror system is seen from the entrance panel. From the top, clockwise, there are the ten spherical sub-mirrors, the two right mirrors, the bottom mirror, and the two left mirrors. At the center, the MAPMTs are visible.

Figure 2.11

supervision of the Frascati and Ferrara experts, the electronic panel was placed in the RICH vessel and tested again to ensure all the readout units worked correctly.

The last step was placing the frontal panel with the aerogel into the detector; the picture in Figure 2.11b was taken during this operation. This operation was particularly critical since the aerogel was resting on its supports. A CCD camera and a small portable light were placed inside the detector to check if any problem occurred during the moving phase. The completed RICH was tested for light leaks, which can cause problems for the SPE, and gas leaks because the inner humidity needs to be minimized to maintain the aerogel properties. At the beginning of June 2022, the RICH was moved into Hall B (Figure 2.13), about 1 km from the clean room, using a truck with a special trolley. The assembly and transportation were made with the detector in a horizontal position; in Hall B, it was rotated to orient it vertically, placing the short side on the bottom and the large on top. Then, it was rotated along the axis which passes through the detector to place it in the final configuration of having the short side on the right, close to the beamline, and the large side on the left. Finally, the RICH was raised to take its place inside the CLAS12 spectrometer. Since the moving phase was another critical step in the installation, the internal CCD camera was used to check again that no problem occurred to the aerogel. Figure 2.14 shows a picture taken inside the RICH after the installation.

Finally, the author was directly involved in cabling the RICH to the infrastructure of the CLAS12 experiment (Figure 2.15a). The picture of the complete array of RICH and LTCC modules of CLAS12 after the second

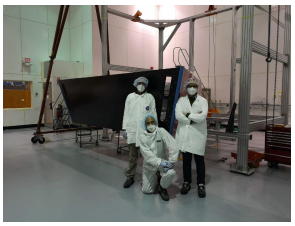

(a) RICH vessel

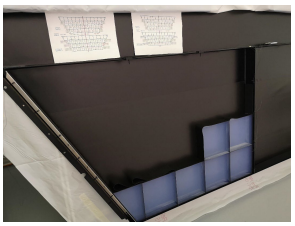

(b) Aerogel preparation

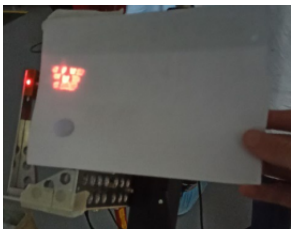

(c) Spherical mirror alignment

(d) Latera mirror assembly

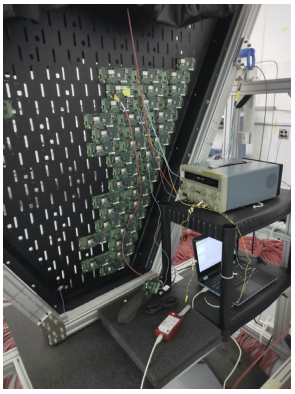

(e) Electronic Panel assembly and testing

(f) Electronic Panel cabling

Figure 2.12

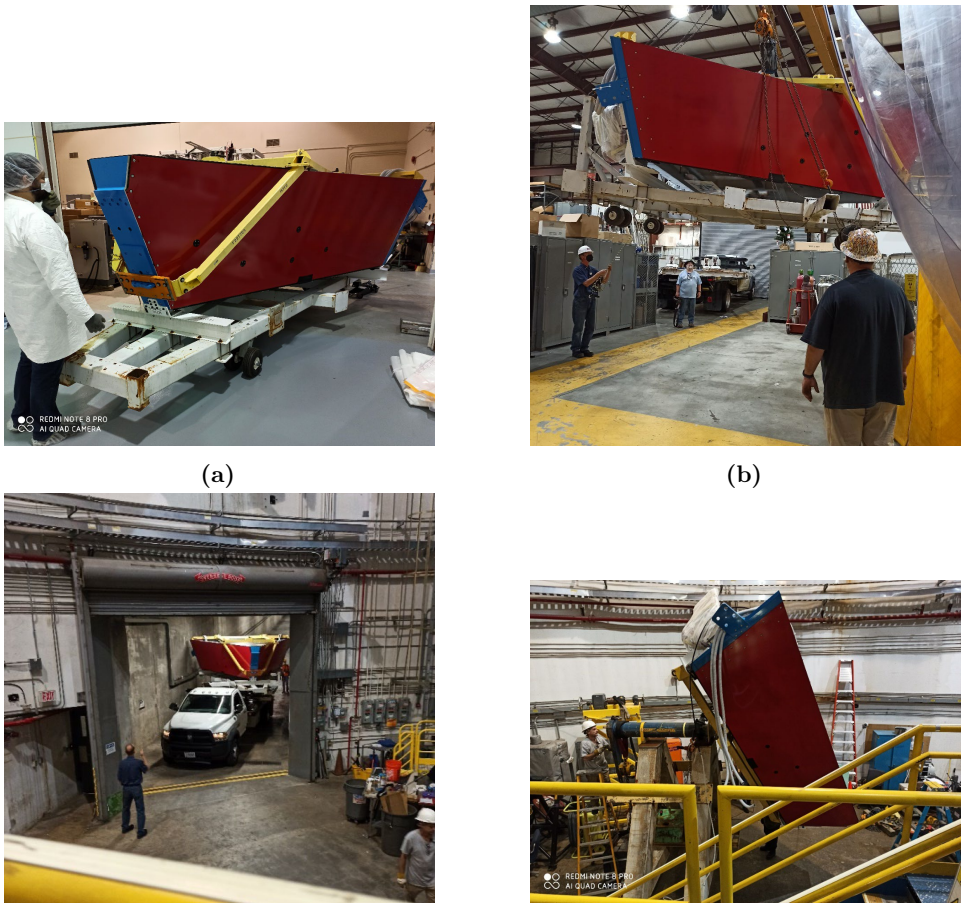

(a) **(b)**

(c) **(d)**

Figure 2.13: Moving of the RICH from the clean room to Hall B.

Figure 2.14: View of the aerogel inside the RICH after ~~placing it~~ in Hall B.

RICH module installation is reported in Figure 2.15b. The RICH was included in the CLAS12 DAQ chain, and all the calibration and control procedures were extended from the first module. The first signals from the two modules are reported in Figures 2.15c and 2.15d.

2.4 RICH ~~efficiency in cleaning the kaon sample~~

The ~~first aim~~ of the RICH was to enhance the kaon identification and improve the pion rejection, ~~then~~ the first efficiency study was performed to evaluate the percentage of ~~correct identification of~~ pions and the percentage of ~~misidentification of pions~~ as ~~a kaon~~, which was not negligible ~~phenomenon~~ using the standard PID of CLAS12. This can be carried out by comparing the missing mass of final states like eH^+X selected using the PID of CLAS12 ~~w~~ithout the RICH ~~or~~ the PID provided by the RICH.

The event selection for this analysis is based on the request that the electron is a trigger particle, its momentum is greater than 1.5 GeV, and ~~both~~ the RICH ~~and~~ CLAS12 identify the hadron. Currently, the range of the hadron polar angle is partially limited because the ~~calibration~~ of part of the spherical sub-mirrors in the reconstruction code has yet to be finalized. The polar angle covers values up to $\sim 15°$, as shown in Figure 2.16.

To evaluate the efficiency, ~~it focuses on~~ the neutron peak ~~of the missing mass at~~ ~~0.94 GeV~~. Indeed, the exclusive final state $e\pi^+n$ is allowed, while t~~he~~ eK^+n is forbidden for strangeness conservation. ~~Then~~, in the missing mass plot of events ~~that include~~ a kaon, the neutron peak should not be present, while it is expected ~~if~~ the selected events include a pion.

A first qualitative idea of the RICH e~~ffectiveness~~ in cleaning the kaon sample ~~can be the~~ plots in Figure 2.17 and Figure 2.18, showing the missing mass of $e\pi^+X$ and eK^+X selected using the CLAS12 ~~o~~r the RICH PID. ~~It is possible to see the neutron peak being present on the plot~~ $eK^{\pm}X$ using the CLAS12 PID, while it is strongly reduced using the RICH PID. In the

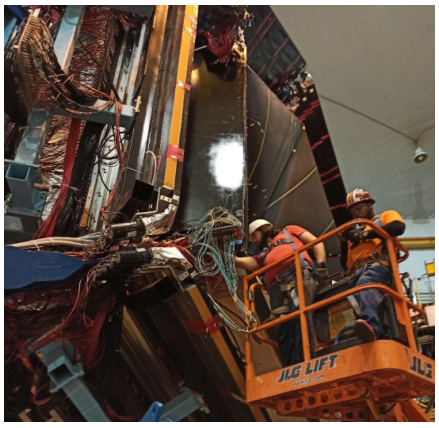

(a) Cabling the RICH

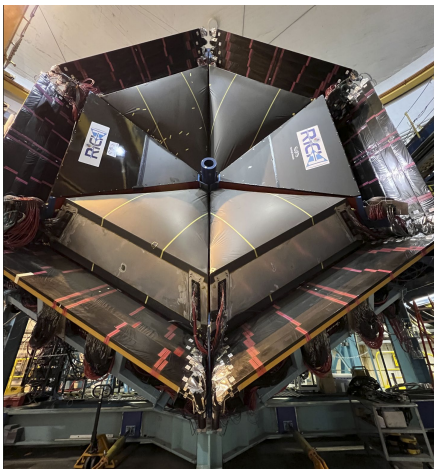

(b) Section of CLAS12 after installing the two modules of the Ring Imaging Cherenkov detector.

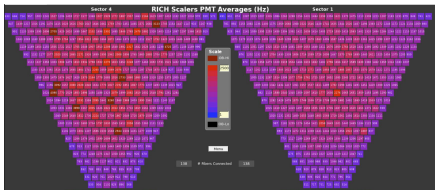

(c) First scalers of the two modules.

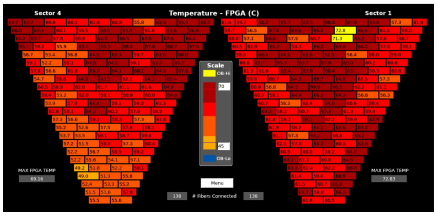

(d) First temperatures of the two modules.

Figure 2.15

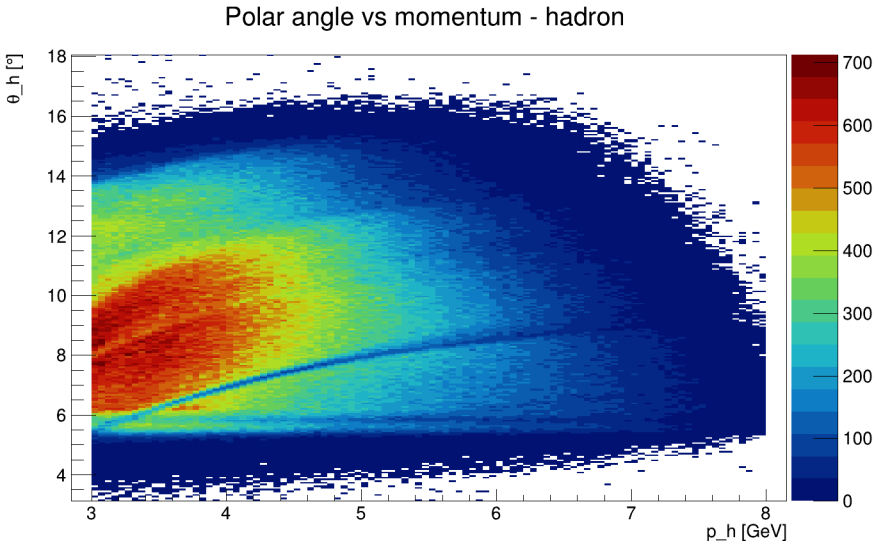

Figure 2.16: Polar angle and momentum of the hadron used for the efficiency study.

$e\pi^+X$ plot, the number of events is larger ~~if~~ using the RICH instead of the CLAS12 PID: this is because a part of the hadrons recognized by CLAS12 as kaons are actually pions, and the RICH correctly identified them. For the same reason, the statistic of the sample selected by the RICH ~~in the missing mass plot of~~ ~~eK^+X~~ is lower than that of the sample identified by CLAS12.

For a quantitative evaluation of the efficiency, it was decided to extract the number of neutrons associated with the peak at 0.94 GeV and to define the pion identification efficiency ($\eta_{\pi\to\pi}$) as

$$\eta_{\pi\to\pi} = \frac{\text{Number of exclusive neutrons in } e\pi^+X \text{ events}}{\text{Number of exclusive neutrons in } (e\pi^+X + eK^+X) \text{ events}} \tag{2.3}$$

and the percentage of pion misidentified as kaon ($\eta_{\pi\to K}$) as

$$\eta_{\pi\to K} = \frac{\text{Number of exclusive neutrons in } eK^+X \text{ events}}{\text{Number of exclusive neutrons in } (e\pi^+X + eK^+X) \text{ events}} \tag{2.4}$$

that substantially means

$$\eta_{\pi\to\pi} = 1 - \eta_{\pi\to K} \tag{2.5}$$

having evaluated that the number of exclusive neutrons in the epX final state is negligible ~~to obtain~~ the accuracy required for this preliminary study.

To estimate the number of neutrons, the missing mass plots were fitted using a Gaussian function for the neutron peak, one or more Gaussian or Breit-Wigner functions for the other peaks, and three ~~different~~ shapes for the

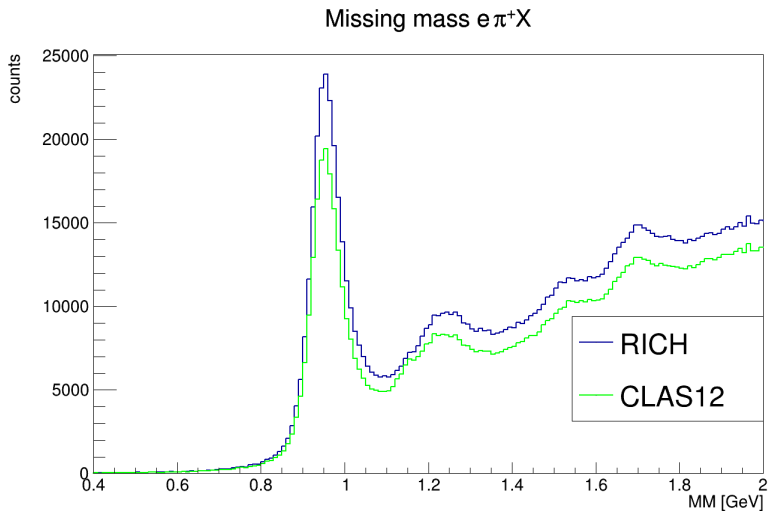

Figure 2.17: Missing mass of final state $e\pi^+X$ ~~for~~ CLAS12 PID (green) ~~and~~ RICH PID (blue). The peak at 0.94 GeV signals the exclusive $e\pi^+n$ final state. The total number of events selected by CLAS12 is less than that selected by RICH because the first misidentified part of the hadrons as if they were kaons.

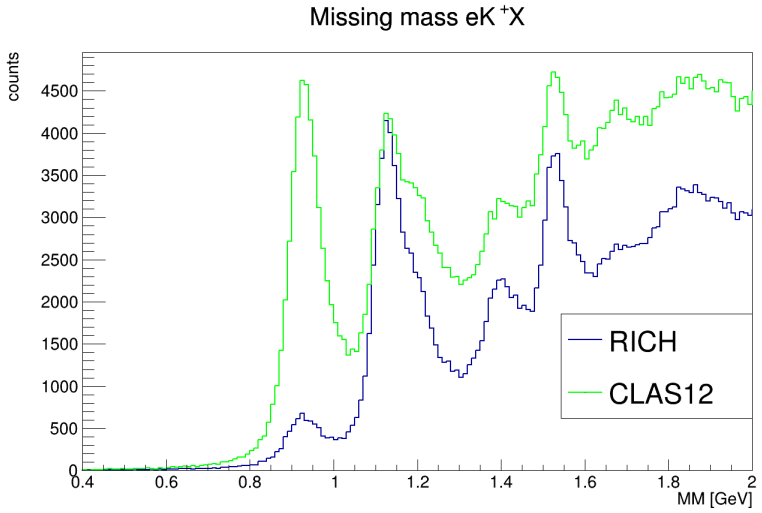

Figure 2.18: Missing mass of final state eK^+X ~~for~~ CLAS12 PID (green) and RICH PID (blue). The clear reduction of the peak at 0.94 GeV ~~using the RI~~CH shows that the number of exclusives state $e\pi^+n$ decreases; this corresponds to a lower number of pions misidentified as kaon, being ~~forbidden~~ the exclusive final state eK^+n. The total number of events selected by CLAS12 is more than that selected by RICH because the first misidentified part of the hadrons as if they were kaons.

SIDIS background distribution: a ~~similar Weibull~~ function, a second-order Chebysev polynomial or a crystal-ball distribution.

$$bkg_{Weib}(x; p_0, p_1, p_2) = p_0 x^{p1-1} \left(-\frac{x}{p_2}\right)^{p_1} \tag{2.6}$$

$$bkg_{Cheb}(x; p_0, p_1, p_2) = p_0 + p_1 x + p_2(2x^2 - 1) \tag{2.7}$$

$$bkg_{Crys}(x; p_0, p_1, p_2, p_3, p_4) = p_0 \cdot \begin{cases} e^{-\frac{1}{2}\left(\frac{x-p_1}{p_2}\right)^2}, & \text{if } \frac{x-p_1}{p_2} > -p_3 \\ \left(\frac{p_4}{|p_3|}\right)^{p_4} \cdot e^{-\frac{|p_3|^2}{2}}, & \text{if } \frac{x-p_1}{p_2} \leq -p_3 \end{cases} \tag{2.8}$$

where p_0, p_1, p_2, p_3, p_4 are the parameters of the background. ~~An~~ example of the fits with the three backgrounds is reported in Figure 2.19, Figure 2.20, and Figure 2.21. Two quantities are shown in the plots: the number of neutrons estimated in the peak (green) and the reduced χ^2 of the fit (black). The former is used to compute the efficiency; the latter permits the evaluation of the fit. In particular, the fit performed with the Chebysev background is not good enough to be used in the efficiency ~~-~~evaluation, while there are no significant differences between the Weibull and Crystalball fits. The number of neutrons is estimated as the integral in ~~-~~$(\mu - 3\sigma, \mu + 3\sigma)$ r~~egion~~ of the Gaussian associated with the ~~-~~peak at 0.94 GeV, ~~-~~the associated error ~~is~~ only the statistical error obtained as the square root of the count. Being the Weibull and Crystalball similar, their average was taken to evaluate $\eta_{\pi\to\pi}$ and $\eta_{\pi\to K}$. The data were binned in the hadron momentum p_H inside the working range of the detector: $(3,4), (4,5), (5,6), (6,8)$. The results are reported in Figure 2.22, and they show that the RICH effectively reduces ~~contamination of pions~~ into the kaon sample. In particular:

- The CLAS12 efficiency on pion detection, obtained using the FTOF and the HTCC, is maximum below the 3 GeV and ~~-~~decreases while the hadron momentum increases;
- The RICH efficiency is essentially flat and close to ~~the 100%~~ in the RICH nominal momentum range
- The ~~contamination of pion into the kaon sample~~ using the CLAS12 PID increases with the momentum of the hadron~~-~~
- The ~~contamination of pion into the kaon sample~~ is strongly reduced using the RICH in the nominal momentum range between 3 and 8 GeV~~-~~

The last point is the main result of this preliminary study on the RICH ~~efficiency~~ because it validates the use of the RICH to select events for kaon Semi-Inclusive Deep Inelastic Scattering studies. The next Chapter will show how the kaon sample can be used to extract a Beam-Spin Asymmetry (BSA), the first step to obtain a new measurement of the nucleon structure functions~~.~~

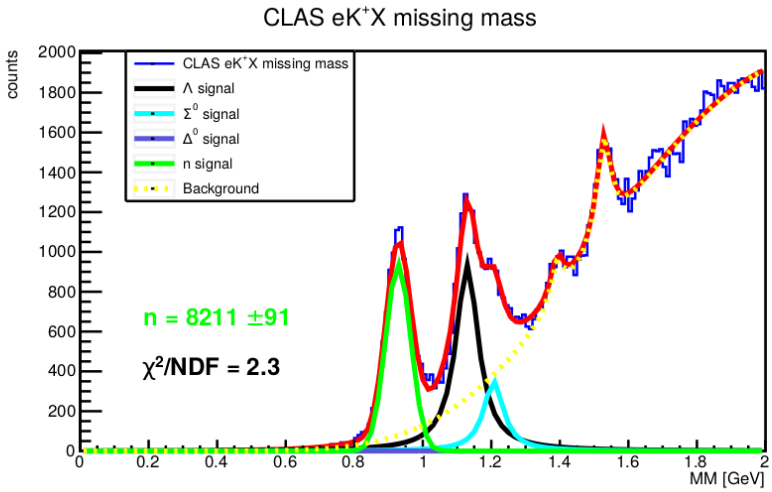

(a) Missing mass of eK^+X selected by CLAS12 PID fitted using Weibull background.

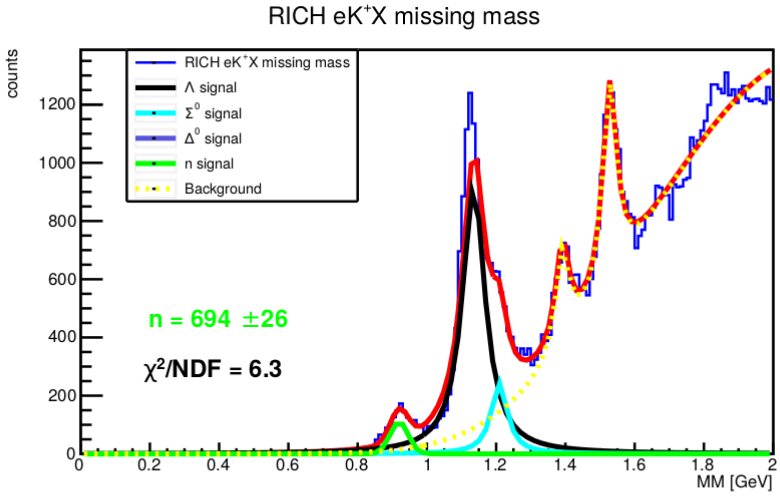

(b) Missing mass of eK^+X selected by RICH fitted using Weibull background

Figure 2.19: Example of missing mass of eK^+X with SIDIS background fitted using the ~~weibull~~ function. The green number is the number of neutrons associated with the peak; the black number is the reduced χ^2 used to evaluate the fit quality.

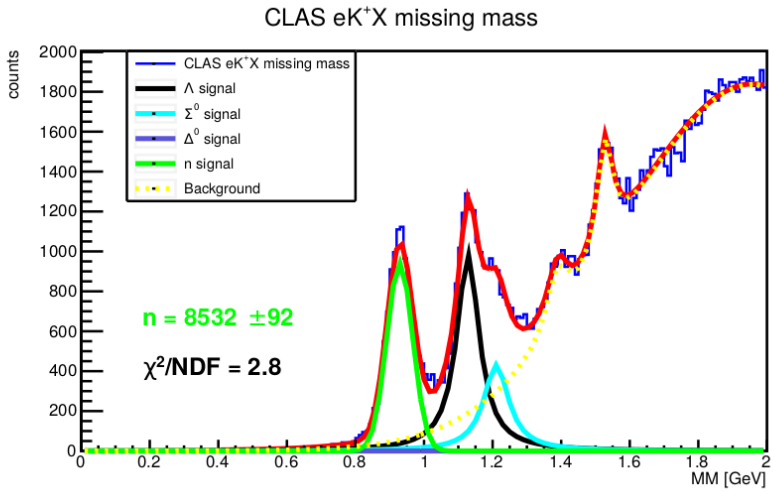

(a) Missing mass of eK^+X selected by CLAS12 PID fitted using Crystalball background.

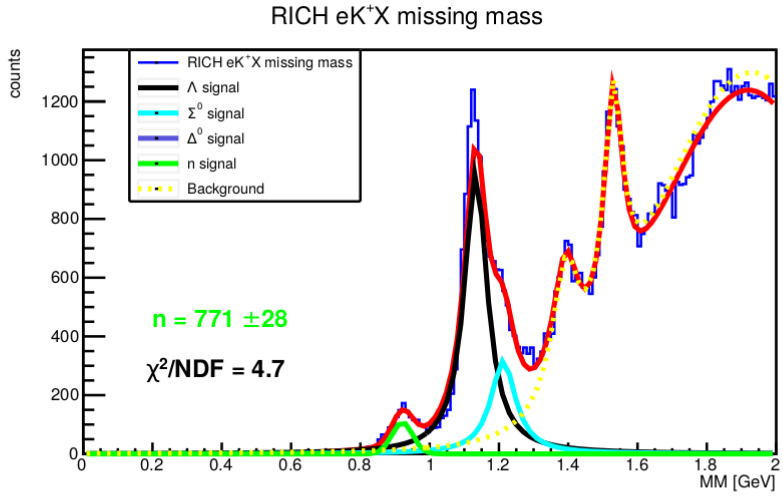

(b) Missing mass of eK^+X selected by RICH fitted using Crystalball background

Figure 2.20: Example of missing mass of eK^+X with SIDIS background fitted using the Crystalball function. The green number is the number of neutrons associated with the peak; the black number is the reduced χ^2 used to evaluate the fit quality.

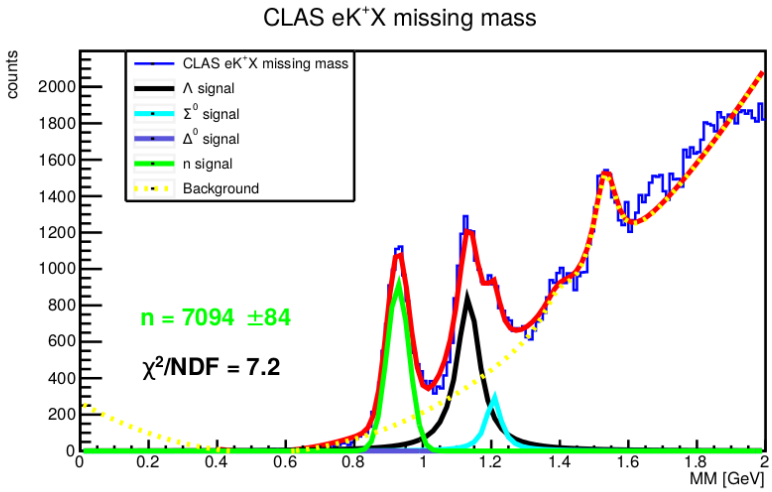

(a) Missing mass of eK^+X selected by CLAS12 PID fitted using Chebysev background.

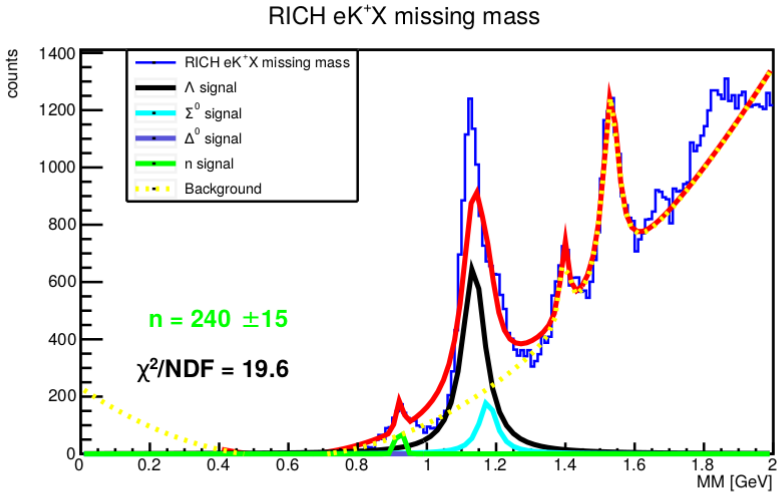

(b) Missing mass of eK^+X selected by RICH fitted using Chebysev background

Figure 2.21: Example of missing mass of eK^+X with SIDIS background fitted using the Chebysev function. The green number is the number of neutrons associated with the peak; the black number is the reduced χ^2 used to evaluate the fit quality.

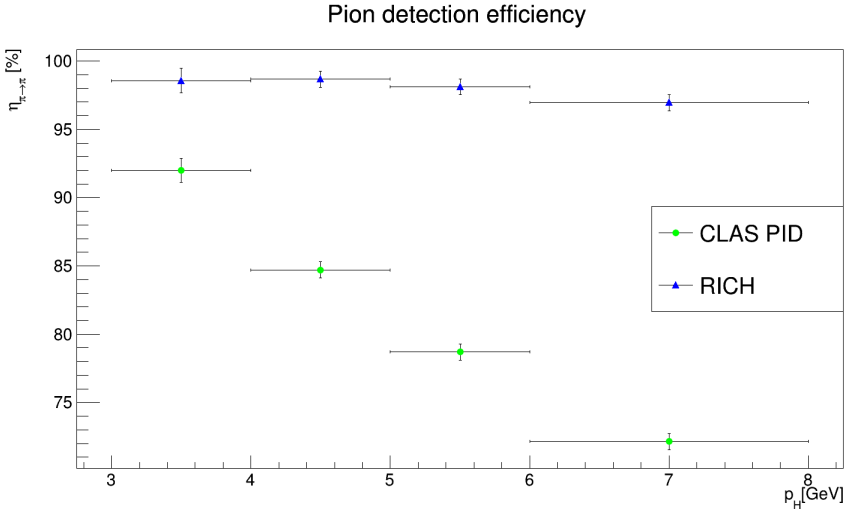

(a) Pion detection efficiency as a function of the hadron momentum.

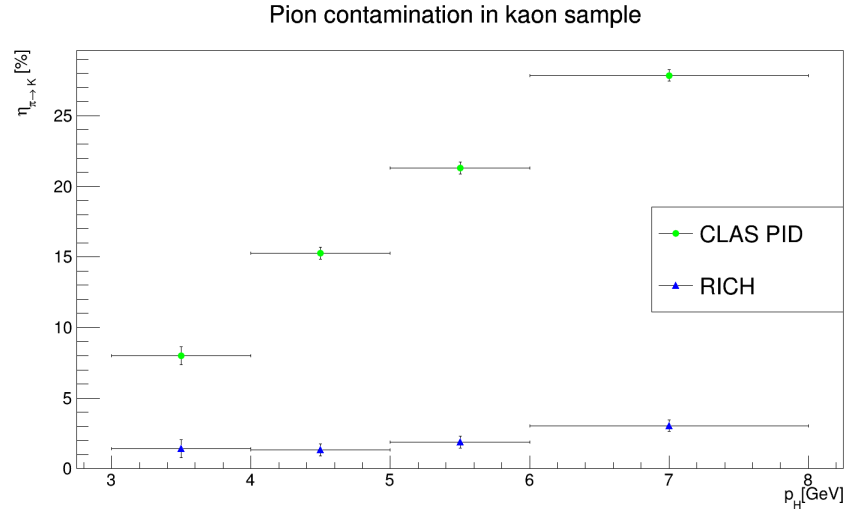

(b) Percentage of pion misidentified as being a kaon as a function of the hadron momentum.

Figure 2.22: Results of the efficiency analysis